

A collider test of nano-Hertz gravitational waves from pulsar timing arrays

Shao-Ping Li^{1,*} and Ke-Pan Xie^{2,†}

¹*Institute of High Energy Physics, Chinese Academy of Sciences, Beijing 100049, China*

²*School of Physics, Beihang University, Beijing 100191, P. R. China*

A cosmic first-order phase transition (FOPT) occurring at MeV-scale provides an attractive explanation for the nano-Hertz gravitational wave (GW) background indicated by the recent pulsar timing array data from the NANOGrav, CPTA, EPTA and PPTA collaborations. We propose this explanation can be further tested at the colliders if the hidden sector couples to the Standard Model sector via Higgs portal. Through a careful analysis of the thermal history of the hidden sector, we demonstrate that in order to successfully explain the observed GW signal, the portal coupling must be sizable that it can be probed through Higgs invisible decay at the LHC or future lepton colliders such as CEPC, ILC, and FCC-ee. Our research offers a promising avenue to uncover the physical origin of the nano-Hertz GWs through particle physics experiments.

I. INTRODUCTION

The observation of gravitational waves (GW) from the merger of binary black hole [1] opens the gate of GW astronomy, enabling the exploration of the Universe through messengers apart from electromagnetic waves and neutrinos. Due to the weakness of gravity, GW can carry information from the very early stage of the Universe, opening the window to detect the important processes prior to the Big Bang nucleosynthesis (BBN) and Cosmic Microwave Background (CMB), and probe new physics beyond the Standard Model (SM). Recently, four pulsar timing array (PTA) collaborations, namely NANOGrav [2], CPTA [3], EPTA [4] and PPTA [5], release their new datasets, showing compelling evidences of a stochastic GW background that peaks at $\mathcal{O}(10^{-8})$ Hz. Intriguingly, Bayesian analysis of the data favors new physics models over the conventional interpretation of inspiraling supermassive black hole binaries [6].

One promising new physics explanation of the nano-Hertz GW is a first-order phase transition (FOPT) that happens at the MeV-scale temperature, which has been studied in the literature [7–13] (also see Refs. [14–21]).¹ In this paper, we consider the GWs induced by the FOPT in a minimal perspective, where the hidden sector only contains a scalar and a dark gauge boson, and it couples to the SM sector via Higgs-portal interactions. We pay particular attention to the connection between the GWs and the particle physics, emphasizing the importance of collider experiments as an efficient probe to identify the physical origin of the nano-Hertz GWs.

The coupling strength between the SM Higgs and a MeV-scale hidden sector has been severely constrained by the LHC data. Such a weak interaction suggests the hidden sector may separate from the SM thermal bath at GeV-scale before the FOPT occurs. Following this decoupling, the hidden sector generally reaches a lower temperature because

the number of SM relativistic degrees of freedom drops significantly at around 100 MeV due to QCD confinement, which in turn reheats the SM sector. Typically, a smaller portal coupling leads to an earlier thermal decoupling and a smaller temperature ratio between the hidden and the SM sectors. However, a smaller temperature ratio reduces the energy fraction of the FOPT in the Universe and hence suppresses the GWs. Consequently, in a vast parameter space, the GW signal has a positive correlation with the Higgs portal strength; especially, we find that the recent reported stochastic GW background requires a sizable portal interaction that can be probed by the Higgs invisible decay at the LHC and future colliders such as CEPC, ILC and FCC-ee.

In this work, we adopt the minimal model with a gauged dark $U(1)_X$ to demonstrate the connection between collider experiments and GWs. In Section II, we introduce the model and establish the framework for the FOPT calculation. Then in Section III, we derive the thermal evolution of hidden sector and point out the relation to Higgs invisible decay. Based on these discussions, we perform the numerical analysis for a few benchmarks present the results in Section IV. Finally, the conclusion is given in Section V.

II. FOPT AND GWS FROM A MINIMAL DARK $U(1)_X$ SCENARIO

As the minimal setup, we consider a new physics hidden sector that is gauged under a dark $U(1)_X$ symmetry. The relevant Lagrangian is

$$\mathcal{L} \supset D_\mu S^\dagger D^\mu S - V(S, H), \quad (1)$$

where $H = (G^+, (h + iG^0)/\sqrt{2})$ is the SM Higgs doublet, $S = (\phi + i\eta)/\sqrt{2}$ is the dark scalar field that is a singlet under the SM gauge group but carries unit charge under the $U(1)_X$, and $D_\mu = \partial_\mu - ig_X A'_\mu$ is the dark covariant derivative with g_X being the gauge coupling and A'_μ the dark gauge boson. The hidden sector is assumed to interact with the SM sector only through the Higgs portal coupling, which is described by the joint potential

$$V(H, S) = \mu_h^2 |H|^2 + \mu_s^2 |S|^2 + \lambda_h |H|^4 + \lambda_s |S|^4 + \lambda_{hs} |H|^2 |S|^2. \quad (2)$$

* spli@ihep.ac.cn

† kpxie@buaa.edu.cn

¹ Other possible explanations include, e.g., models involving domain walls [22–25], cosmic strings [26–29], inflationary or scalar-induced physics [30–33], black holes [34–42], etc [43–45].

The scalars develop vacuum expectation values (VEVs) at $(h, \phi) = (v_{\text{ew}}, v_s)$ which breaks the electroweak (EW) and $U(1)_X$ gauge symmetries. The dark gauge boson then acquires a mass $m_{A'} = g_X v_s$.

The coefficients $\{\mu_h^2, \mu_s^2, \lambda_h, \lambda_s, \lambda_{hs}\}$ in potential Eq. (2) can be re-parametrized using the physical observables $\{m_h, v_{\text{ew}}, m_\phi, v_s, \theta\}$, where θ is the mixing angle between the Higgs boson h and the dark scalar ϕ . Given $m_h = 125.09$ GeV and $v_{\text{ew}} = 246$ GeV, there are three free parameters in $V(H, S)$, and $|\theta| \ll 1$ is required by the Higgs and EW measurements. The details of the re-parametrization of the potential can be found in Appendix A. Here we focus on the MeV-scale hidden FOPT well below the EW symmetry breaking and hence $h \rightarrow v_{\text{ew}}$. Therefore, the tree-level potential at zero temperature can be matched to

$$V_0(\phi) \approx \frac{m_\phi^2}{8v_s^2} (\phi^2 - v_s^2)^2, \quad (3)$$

along the ϕ -direction.

To study the dynamics of hidden sector in the hot and dense environment of the early Universe, we need take into account the finite-temperature corrections. Here we denote the temperatures in the hidden and SM sectors as T' and T , respectively, and allow $\xi \equiv T'/T$ to deviate from 1, and ξ itself also varies during the cosmic evolution. The effective ϕ -potential at finite temperatures is

$$V_{\text{eff}}(\phi, T') = V_0(\phi) + V_{\text{CW}}(\phi) + V_T(\phi, T'), \quad (4)$$

where $V_{\text{CW}} \equiv V_1(\phi) + \delta V(\phi)$ is the Coleman-Weinberg potential at zero temperature with the counterterm $\delta V(\phi)$ attached, and $V_T(\phi, T') \equiv V_{1T}(\phi, T') + V_{\text{daisy}}(\phi, T')$ is the one-loop thermal correction plus the daisy resummation term. See Appendix B for the complete expressions.

FOPT occurs when the Universe transitions from a false vacuum (local minimum) to a true vacuum (global minimum). Initially, the Universe retains at $\phi = 0$ due to the behavior of $V_{\text{eff}}(\phi, T') \sim (-m_\phi^2 + g_X^2 T'^2/2)\phi^2/4$ at $\phi \sim 0$, which exhibits a valley for high enough T_h . The $U(1)_X$ symmetry is preserved at this stage. However, as T' decreases, another local minimum at $\phi \neq 0$ emerges and becomes the true vacuum. In certain parameter space, a barrier formed mainly by A' in the thermal loop separates the two minima, preventing a smooth transition. In such cases, the Universe undergoes quantum tunneling to the true vacuum, resulting in a $U(1)_X$ -breaking FOPT with bubble nucleation and expansion dynamics.

We briefly describe the FOPT and GW calculation framework. Bubbles containing the $U(1)_X$ -breaking vacuum start to nucleate at T'_n when the decay probability in a Hubble volume and Hubble time reaches $\mathcal{O}(1)$, i.e.

$$\Gamma(T'_n) H^{-4}(T'_n) \approx 1, \quad (5)$$

where decay rate per unit volume and unit time is

$$\Gamma(T') \approx T'^4 \left(\frac{S_3}{2\pi T'} \right)^{3/2} e^{-S_3/T'}, \quad (6)$$

derived by the T' -dependent action S_3 of the $O(3)$ -symmetric bounce solution [46]. The Hubble constant is dominated by the SM sector, i.e.

$$H(T) \approx 2\pi \sqrt{\frac{\pi g_*(T)}{45}} \frac{T^2}{M_{\text{Pl}}}, \quad (7)$$

where $M_{\text{Pl}} = 1.22 \times 10^{19}$ GeV is the Planck mass and $g_*(T)$ is the number of relativistic degrees of freedom (d.o.f.) in the SM sector. We have assumed a mild FOPT such that the Hubble constant is dominated by the radiation energy throughout the transition, and hence nucleation usually ensures the completion of the FOPT [47]. Therefore, Eq. (5) can be adopted as the FOPT criterion, and numerically it implies

$$\frac{S_3}{T'_n} \approx 4 \log \left(\frac{1}{4\pi} \sqrt{\frac{45}{\pi g_*(T'_n)}} \frac{M_{\text{Pl}}}{T'_n} \xi_n^2 \right). \quad (8)$$

Note that the right-hand side contains both T_n and T'_n , and they are related by ξ_n , which is the ξ value at nucleation. For an MeV-scale FOPT, $g_*(T_n) = 10.75$ and $S_3/T'_n \approx 190$.

FOPTs source stochastic GWs via bubble collisions, sound waves and turbulence in the plasma [48]. The key variables describing the GW spectrum are $\{\alpha, \beta/H_n, T_n, v_w\}$, where

$$\alpha = \frac{1}{g_*(T_n) \pi^2 T_n^4 / 30} \left(T' \frac{\partial \Delta V_{\text{eff}}}{\partial T'} - \Delta V_{\text{eff}} \right) \Big|_{T'_n}, \quad (9)$$

with $\Delta V_{\text{eff}} < 0$ being energy difference between the true and false vacua. In other words, α is the ratio of FOPT latent heat to the radiation energy, and it can be factorized as

$$\alpha = \frac{g'_*(T'_n)}{g_*(T_n)} \alpha_h \times \xi_h^4, \quad (10)$$

where α_h is the latent heat over the hidden radiation energy, and $g'_*(T'_n) = 2 + 3 = 5$ is the number of hidden relativistic d.o.f. By this factorization, we can calculate α_h with the hidden sector observables alone and then convert it to α for GW calculation. Normally, $\alpha_h \lesssim 1$ for a non-supercooled FOPT. On the other hand, the β/H_n parameter, defined as the inverse ratio of the FOPT duration to the Hubble time, can be calculated using only the hidden observables

$$\frac{\beta}{H_n} = T'_n \frac{d(S_3/T')}{dT'} \Big|_{T'_n}, \quad (11)$$

due to the cancellation of ξ_n factor in the definition [49].

After nucleation, the bubbles undergo an accelerating expansion driven by the vacuum pressure. In the case of a mild FOPT where $\alpha \lesssim 1$, the friction force exerted by A' and ϕ in the plasma quickly balances the vacuum pressure, resulting in a terminal wall velocity $v_w < 1$. As a result, most of the vacuum energy released during the FOPT is transferred to plasma motion. Therefore, GWs are primarily generated by sound waves, with turbulence playing a secondary role, while the contribution from bubble collisions is negligible [50].

After the cosmological redshift, the GW spectrum today can be described by the energy fraction

$$\Omega_{\text{GW}}(f) = \frac{1}{\rho_c} \frac{d\rho_{\text{GW}}}{d \log f}, \quad (12)$$

where ρ_{GW} and ρ_c are the GW and the current Universe energy density, respectively. Following Ref. [51], we can write the sound wave contribution as [52]

$$\begin{aligned} \Omega_{\text{sw}}(f)h^2 &= 5.71 \times 10^{-8} v_w \left(\frac{\kappa_V \alpha}{1 + \alpha} \right)^2 \left(\frac{\beta/H_n}{100} \right)^{-1} \\ &\times \left(\frac{g_*}{10} \right)^{-1/3} \left(\frac{f}{f_{\text{sw}}} \right)^3 \left(\frac{7}{4 + 3(f/f_{\text{sw}})^2} \right)^{7/2}, \quad (13) \end{aligned}$$

where κ_V is the fraction of vacuum energy that goes to surrounding plasma, which can be derived by resolving the hydrodynamic motion of the fluid [53], and

$$\begin{aligned} f_{\text{sw}} &= 1.3 \times 10^{-8} \text{ Hz} \\ &\times \frac{1}{v_w} \left(\frac{\beta/H_n}{100} \right) \left(\frac{T_n}{\text{MeV}} \right) \left(\frac{g_*}{10} \right)^{1/6}, \quad (14) \end{aligned}$$

is the peak frequency, from which we can clearly see the relation between the reported $f_{\text{sw}} \sim 10^{-8}$ Hz signal and a MeV-scale T_n . To include the finite lifetime of sound wave period, we multiply Eq. (13) with an extra factor $H\tau_{\text{sw}} \leq 1$ [54]. The sub-leading turbulence contribution is calculated using numerical results [55].

III. THERMAL HISTORY OF THE HIDDEN SECTOR

The Higgs-portal interactions mediated by λ_{hs} in Eq. (2) ensure that the hidden sector remains in equilibrium with the SM sector at high temperatures. In the temperature range $\text{MeV} \lesssim T \ll 100 \text{ GeV}$, specifically after the EW symmetry breaking and before the FOPT, thermal contact is maintained through the Higgs induced process: $SS^\dagger \rightarrow h^* \rightarrow \text{SM particle pairs}$. The thermally averaged rate for this process, denoted as Γ_{SS^\dagger} , scales as $\lambda_{hs}^2 T^5/m_h^4$, so that it decreases more rapidly than the Hubble expansion rate $H(T) \propto T^2/M_{\text{Pl}}$. When Γ_{SS^\dagger}/H drops below 1, the hidden sector decouples from the SM plasma and evolves with its own temperature T' , which differs from the SM temperature T .

After the decoupling, the hidden sector typically has a lower temperature $T' < T$. This is because the SM sector is reheated when there is a particle species that becomes non-relativistic and injects energy to the plasma. Such an effect is prominent especially at $T \sim 100 \text{ MeV}$ when the quarks and gluons are confined into hadrons, and $g_*(T)$ drops drastically from 61.75 to 10.75. In contrast, the hidden sector does not have such reheating effects as it contains only S and A . Therefore $\xi_n \equiv \xi(T_n) < 1$, which suppresses the α parameter by a factor of ξ_n^4 , as indicated by Eq. (10); this further suppresses the GW peak signal by

$$\Omega_{\text{sw}}(f_{\text{sw}}) \rightarrow \xi_n^8 \Omega_{\text{sw}}(f_{\text{sw}}), \quad (15)$$

which can be inferred from Eq. (13). Therefore, a moderate $\xi_n \sim 1/2$ can already suppress the GW signal strength by a factor of 10^{-3} , and hence the deriving ξ_n is very important in the calculation of the FOPT GW spectrum.

ξ_n is determined by evolving the hidden and SM sectors below the decoupling temperature T_{dec} , which is resolved by

$$\Gamma_{SS^\dagger}(T_{\text{dec}}) = H(T_{\text{dec}}). \quad (16)$$

below this temperature, the above equality becomes a less-than sign, and the thermal contact is lost. When resolving T_{dec} , we consider the annihilation of $SS^\dagger \rightarrow h^* \rightarrow$ a pair of SM particles including electrons, muons, pions and kaons, and the relevant meson interaction vertices are taken from Ref. [56]. Below T_{dec} , the two sectors evolve separately and the entropy in either sector conserves, and hence

$$\xi(T) = \left(\frac{g_*(T)}{g_*(T_{\text{dec}})} \frac{g'_*(T_{\text{dec}})}{g'_*(T')} \right)^{1/3}, \quad (17)$$

which is smaller than 1 when $T < T_{\text{dec}}$ and $g_*(T)$ drops below $g_*(T_{\text{dec}})$.

The zero-temperature scalar-Higgs mixing angle θ is crucial in evaluating T_{dec} , as the relevant annihilation processes are mediated by an off-shell Higgs boson and hence has a $\Gamma_{SS^\dagger} \sim \lambda_{hs}^2 T^5/m_h^4$ scaling, while λ_{hs} is related to the zero-temperature via

$$\lambda_{hs} \approx \frac{m_\phi^2 - m_h^2}{v_{\text{EW}} v_s} \theta. \quad (18)$$

See also the details in Appendix A. In general, a larger θ results in a larger annihilation rate and consequently a T_{dec} closer to T_n , which then gives a larger ξ_n , relaxing the suppression on the GW signals. Therefore, the observed GW background favors a large θ . However, θ also controls the Higgs exotic decay partial width by

$$\Gamma(h \rightarrow 2\phi) = \frac{\theta^2 m_h}{32\pi} \frac{m_h^2}{v_s^2} \left(1 + \frac{2m_\phi^2}{m_h^2} \right)^2 \sqrt{1 - \frac{4m_\phi^2}{m_h^2}}, \quad (19)$$

and hence is stringently constrained by current experiments.

ϕ is not a stable particle in our model, and it decays via the mixing with the Higgs boson. For MeV-scale ϕ , the decay to e^+e^- final state dominates, and the corresponding lifetime of ϕ , as we will see in the next section, is $\mathcal{O}(1)$ s, resulting in Higgs invisible decay signals at colliders. Currently, the CMS collaboration sets $\text{BR}(h \rightarrow 2\phi) < 0.19$ at 90% C.L. [57] based on the 13 TeV LHC data, and this is interpreted as an upper bound of $|\theta| \lesssim 10^{-5}$. Future detection from the HL-LHC can reach $\text{BR}(h \rightarrow 2\phi) \approx 0.019$ [58], and moreover, the future Higgs factories such as CEPC, ILC or FCC-ee can reach $\text{BR}(h \rightarrow 2\phi) \sim 10^{-3}$ [59–61], increasing the sensitivity of θ by at least an order of magnitude. These collider experiments can efficiently probe the parameter space favored by the nano-Hertz GW signals indicated by the PTA data, as we show in the next section.

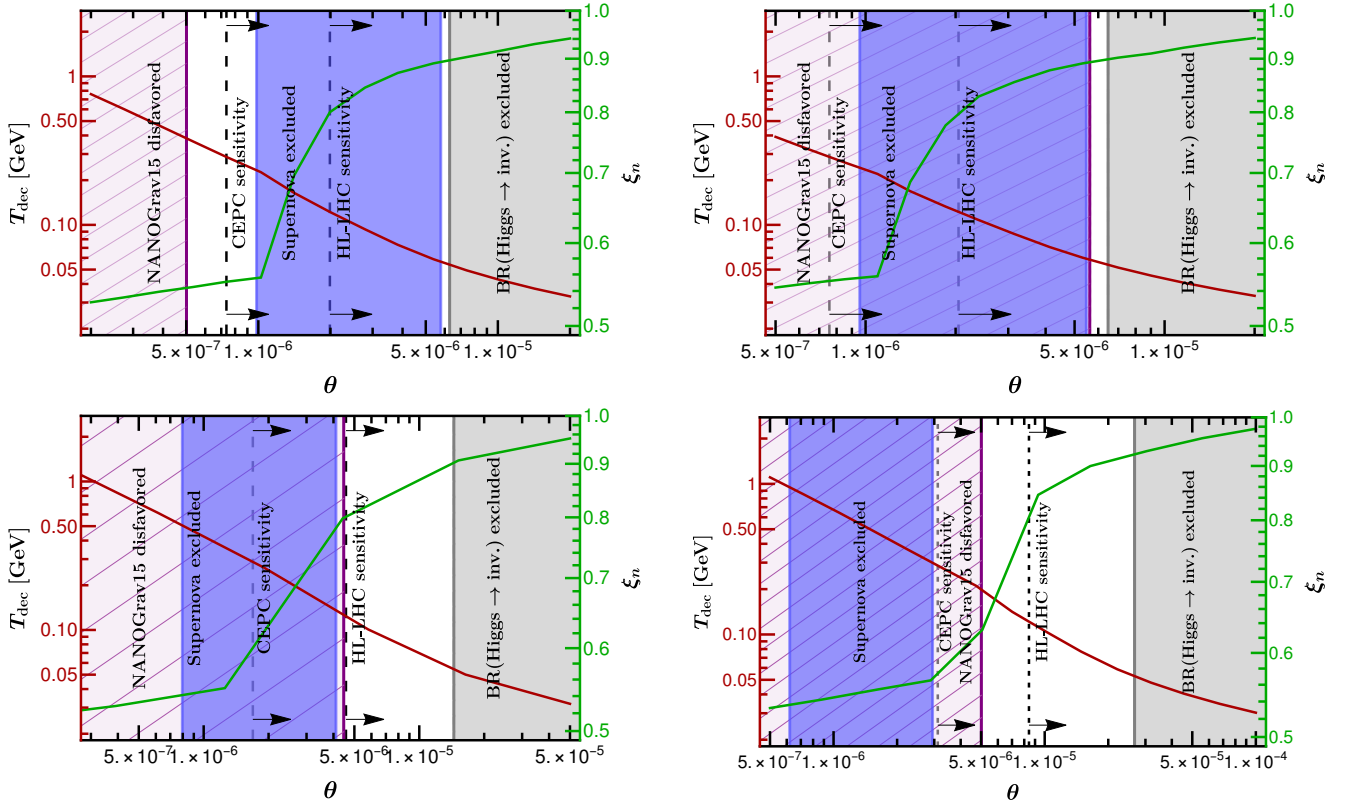


FIG. 1. Four BPs: BP1 (top left), BP2 (top right), BP3 (bottom left) and BP4 (bottom right). The T_{dec} and ξ_n as functions of θ are shown as red and green curves, respectively. The region disfavored by the PTA data is covered by mesh, while the region excluded by the LHC data is covered by gray. The supernova-excluded region is colored by blue. The projected reach of HL-LHC and CEPC are shown as gray dashed vertical lines.

IV. TESTING THE ORIGIN OF GWS AT COLLIDERS

To quantitatively show our results, for a given parameter set of (m_ϕ, v_s, g_X) , we use the Python package `cosmoTransitions` [62] to calculate the bounce action S_3 and derive T'_n via Eq. (8). Then a scan of θ is performed to determine T_{dec} via Eq. (16) and hence ξ_n via Eq. (17). We choose four benchmark points (BPs) as listed in Table I, and plot T_{dec} and ξ_n as functions of θ in Fig. 1, from which we immediately see the expected negative (positive) correlation of T_{dec} (ξ_n) to θ . For the parameter space of interest, T_{dec} is at GeV to MeV scale, while ξ_n varies from 0.5 to 1. We also notice that ξ_n changes rapidly when T_{dec} crosses ~ 100 MeV due to the variation of $g_*(T)$ caused by QCD confinement, which can be understood from Eq. (17).

Given ξ_n , we can calculate the GW spectrum as described in Section II, mainly based on the discussions around Eq. (13). The predicted GW signal curve can then be compared with the PTA data from the NANOGrav [2] and CPTA [3] collaborations. For the former, we adopt the $f\text{-}\Omega_{\text{GW}}(f)h^2$ data points from Ref. [6]; while for the latter, we use the best fit point of $f = 14$ nHz and transfer $\log_{10}A = -14.4^{+1.0}_{-2.8}$ [3] into $\Omega_{\text{GW}}h^2$ as an estimate. By varying θ , we see the expected ξ_n^8 suppression effect on the GW signal strength. Hence the parameter space favored by the PTA data

	m_ϕ [MeV]	v_s [MeV]	g_X	θ_{min}	α	β/H_n	T'_n [MeV]
BP1	5.39	31.4	0.949	5.01×10^{-7}	0.294	52.2	3.51
BP2	7.07	32.3	1.07	5.62×10^{-6}	0.342	17.7	6.96
BP3	16.3	72.3	1.09	4.47×10^{-6}	0.248	12.6	15.0
BP4	31.2	133	1.13	5.01×10^{-6}	0.195	16.8	22.2

TABLE I. The chosen BPs with the (m_ϕ, v_s, g_X) values. θ_{min} is the minimal θ favored by the GW data, and the subsequent $(\alpha, \beta/H_n, T'_n)$ is evaluated at θ_{min} .

exhibits a lower limit for θ , as shown in Fig. 1, where the disfavored regions are covered by mesh. The GW spectra of the four BPs with the minimal allowed θ are plotted in Fig. 2, and the corresponding parameters α , β/H_n and T'_n are listed in Table I. As mentioned before, current LHC measurements of Higgs invisible decay set an upper bound $|\theta| \lesssim 10^{-5}$ on the mixing angle, and this is shown as the gray shaded regions in Fig. 1.

The FOPT temperatures of our BPs are typically larger than a few MeV, and thus are safe under the BBN and CMB constraints [63, 64]. The constraints from ultra-compact minihalo (UCMH) abundance [65, 66] can also be relaxed by adopting a conservative value of the redshift $z_c = 1000$ of the last formation of UCHM. Besides, astrophysical and cosmological constraints due to the light scalar ϕ interacting

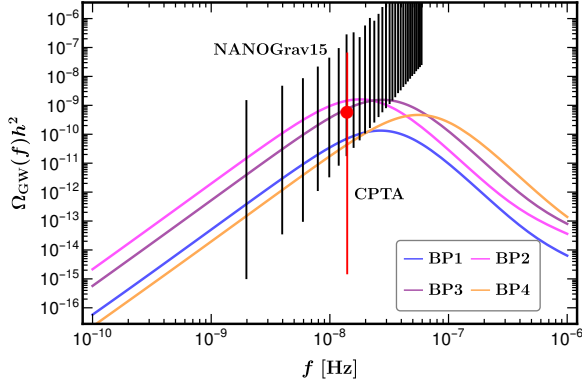


FIG. 2. GW spectra for the BPs in Table I. The PTA data are explained in the main text.

with the SM particles also come into effect. Such a light ϕ boson can be produced in stellar objects, such as the supernova. For a much smaller θ , the produced ϕ can carry energy of the supernova and escape without being trapped, but when θ is much larger, the dark scalar is trapped within the supernova. Therefore, there is a bound of θ from the supernova luminosity constraints [67], as covered by the blue shaded regions. In addition, a light scalar can affect the BBN process, which in general depends on the scalar mass, the lifetime τ_ϕ and the number density at decay. Following the analysis of Refs. [68, 69], we calculate for each BP the parameter set of $(m_\phi, \tau_\phi, n_\phi)$ and compare with the limits inferred therein. We find that all the four BPs are allowed by the BBN constraints.

Finally, the regions that are not covered by neither mesh nor colors are viable for explaining the nano-Hertz GW background while being consistent with existing bounds from particle physics, astrophysics and cosmology, opening a window for future experimental exploration.

We represent the projected reach of $\text{BR}(h \rightarrow \phi\phi)$ at the HL-LHC and the CEPC as vertical dashed lines, with 1.9% [58] and 0.26% [59] respectively. The HL-LHC has the capability to explore the entire GW-favored parameter space for BP1 and BP2, as well as a portion of BP3 and BP4. The future CEPC can probe entire allowed parameter space for each of the BPs, and anticipated sensitivities of the ILC and the FCC-ee are comparable. Hence, both ongoing and forthcoming collider experiments serve as highly effective means to investigate the physics associated with the nano-Hertz GW background.

V. CONCLUSION

In this study, we propose a collider test to the nano-Hertz GW signals reported by the recent PTA experiments. Our idea is based on the extensively-studied Higgs-portal model, which consists of a hidden sector that is gauged under a dark $U(1)'$. We demonstrate that the explanation of the PTA data requires a sizable Higgs portal coupling, which results in a $h \rightarrow \phi\phi$

exotic decay that leads to an Higgs invisible decay final state, and can be probed at the colliders. By choosing several BPs as examples, we show that the HL-LHC is able to efficiently probe the parameter space required by the PTA data, while the future lepton colliders such as CEPC can cover almost all the parameter space of interest. Our research shows the great importance of collider experiments in identifying the origin of the stochastic GW background.

ACKNOWLEDGEMENTS

We would like to thank Jing Liu and Mengchao Zhang for very useful discussions. S. Li is supported in part by the National Natural Science Foundation of China under grant No. 12141501.

Appendix A: The re-parametrization of the joint potential

In the unitary gauge, $H \rightarrow h/\sqrt{2}$ and $S \rightarrow \phi/\sqrt{2}$, the potential is rewritten as

$$V(h, \phi) = \frac{\mu_h^2}{2} h^2 + \frac{\lambda_h}{4} h^4 + \frac{\mu_s^2}{2} \phi^2 + \frac{\lambda_s}{4} \phi^4 + \frac{\lambda_{hs}}{4} h^2 \phi^2, \quad (\text{A1})$$

which is minimized at the vacuum $(h, \phi) = (v_{\text{ew}}, v_s)$. Given the mass eigenvalues m_h , m_ϕ and the mixing angle θ , the coefficients in Eq. (A1) can be expressed as

$$\mu_{h,s}^2 = -\frac{1}{4} \left[m_h^2 + m_\phi^2 \mp (m_\phi^2 - m_h^2) \left(\cos 2\theta \mp \left(\frac{v_s}{v_{\text{ew}}} \right)^{\pm 1} \sin 2\theta \right) \right], \quad (\text{A2})$$

and

$$\begin{aligned} \lambda_h &= \frac{m_h^2 + m_\phi^2 - (m_\phi^2 - m_h^2) \cos 2\theta}{4v_{\text{ew}}^2}, \\ \lambda_s &= \frac{m_h^2 + m_\phi^2 + (m_\phi^2 - m_h^2) \cos 2\theta}{4v_s^2}, \\ \lambda_{hs} &= \frac{(m_\phi^2 - m_h^2) \sin 2\theta}{2v_{\text{ew}}v_s}. \end{aligned} \quad (\text{A3})$$

For small mixing angle $|\theta| \ll 1$, the interaction vertices can be read from the following interaction Lagrangian

$$\begin{aligned} \mathcal{L}_3 \approx & -\frac{m_h^2}{2v_{\text{ew}}} h^3 + \frac{2m_h^2 + m_\phi^2}{2v_{\text{ew}}} \theta h^2 \phi \\ & + \frac{m_h^2 + 2m_\phi^2}{2v_s} \theta h \phi^2 - \frac{m_\phi^2}{2v_s} \phi^3, \end{aligned} \quad (\text{A4})$$

$$\begin{aligned} \mathcal{L}_4 \approx & -\frac{m_h^2}{8v_{\text{ew}}^2} h^4 - \frac{m_h^2}{2v_{\text{ew}}^2} \theta h^3 \phi - \frac{m_\phi^2 - m_h^2}{4v_{\text{ew}}v_s} \theta h^2 \phi^2 \\ & + \frac{m_\phi^2}{2v_s^2} \theta h \phi^3 - \frac{m_\phi^2}{8v_s^2} \phi^4, \end{aligned} \quad (\text{A5})$$

in which h and ϕ should be understood as physical particles.

Appendix B: The complete expression of the $V_T(\phi, T)$

The finite temperature potential of ϕ consists of zero-temperature tree level potential $V_0(\phi)$ as given in Eq. (3), the one-loop Coleman-Weinberg correction

$$V_1(\phi) = \sum_{i=\phi, A'} \frac{n_i M_i^4(\phi)}{64\pi^2} \left(\log \frac{M_i^2(\phi)}{\mu_R^2} - C_i \right), \quad (\text{B1})$$

where $\mu_R = 10$ MeV is the renormalization scale,

$$M_\phi^2(\phi) = -\frac{m_\phi^2}{2} + \frac{3m_\phi^2}{2v_s^2} \phi^2, \quad M_{A'}(\phi) = g_X \phi, \quad (\text{B2})$$

are the field-dependent masses, $n_{\phi, A'} = 1, 3$ and $C_{\phi, A'} = 3/2, 5/6$, respectively. Note that the contribution from the Goldstone η is neglected to avoid the IR divergence [70]. The counter term $\delta V(\phi) \equiv \delta\mu_s^2 \phi^2/2 + \delta\lambda_s \phi^4/4$ is determined by the condition that one-loop zero temperature potential $V_0(\phi) + V_1(\phi) + \delta V(\phi)$ should still have a VEV at $\langle \phi \rangle = v_s$ with a mass eigenvalue m_ϕ .

The thermal correction at one-loop level is given by

$$V_{T1}(\phi, T') = \sum_{i=\phi, \eta, A'} \frac{n_i T'^4}{2\pi^2} J_B \left(\frac{M_i^2(\phi)}{T'^2} \right), \quad (\text{B3})$$

where $n_\eta = 1$ and $M_\eta^2(\phi) = -m_\phi^2(1 - \phi^2/v_s^2)/2$, and the Bose thermal integral

$$J_B(y) = \int_0^\infty x^2 dx \log(1 - e^{-\sqrt{x^2+y}}).$$

The thermal correction is dominated by the A' contribution, as $g_X^2 \gg \lambda_s$ in the parameter space of interest. The last term in Eq. (4), i.e. the daisy resummation, is

$$V_{\text{daisy}}(\phi, T') = -\frac{g_X^3 T'}{12\pi} \left((\phi^2 + T'^2)^{3/2} - \phi^3 \right), \quad (\text{B4})$$

where the sub-leading contributions from ϕ and η are dropped.

-
- [1] B. P. Abbott et al. (LIGO Scientific, Virgo), *Phys. Rev. Lett.* **116**, 061102 (2016), 1602.03837.
- [2] G. Agazie et al. (NANOGrav), *Astrophys. J. Lett.* **951** (2023), 2306.16213.
- [3] H. Xu et al. (2023), 2306.16216.
- [4] J. Antoniadis et al. (2023), 2306.16214.
- [5] D. J. Reardon et al. (2023), 2306.16215.
- [6] A. Afzal et al. (NANOGrav) (2023), 2306.16219.
- [7] C. Han, K.-P. Xie, J. M. Yang, and M. Zhang (2023), 2306.16966.
- [8] E. Megias, G. Nardini, and M. Quiros (2023), 2306.17071.
- [9] K. Fujikura, S. Girmohanta, Y. Nakai, and M. Suzuki (2023), 2306.17086.
- [10] L. Zu, C. Zhang, Y.-Y. Li, Y.-C. Gu, Y.-L. S. Tsai, and Y.-Z. Fan (2023), 2306.16769.
- [11] P. Athron, A. Fowlie, C.-T. Lu, L. Morris, L. Wu, Z. Xu, and Y. Wu (2023), 2306.17239.
- [12] A. Yang, J. Ma, S. Jiang, and F. P. Huang (2023), 2306.17827.
- [13] A. Addazi, Y.-F. Cai, A. Marciano, and L. Visinelli (2023), 2306.17205.
- [14] A. Addazi, Y.-F. Cai, Q. Gan, A. Marciano, and K. Zeng, *Sci. China Phys. Mech. Astron.* **64**, 290411 (2021), 2009.10327.
- [15] L. Bian, R.-G. Cai, J. Liu, X.-Y. Yang, and R. Zhou, *Phys. Rev. D* **103**, L081301 (2021), 2009.13893.
- [16] Y. Nakai, M. Suzuki, F. Takahashi, and M. Yamada, *Phys. Lett. B* **816**, 136238 (2021), 2009.09754.
- [17] W. Ratzinger and P. Schwaller, *SciPost Phys.* **10**, 047 (2021), 2009.11875.
- [18] D. Borah, A. Dasgupta, and S. K. Kang, *JCAP* **12**, 039 (2021), 2109.11558.
- [19] K. Freese and M. W. Winkler, *Phys. Rev. D* **106**, 103523 (2022), 2208.03330.
- [20] T. Bringmann, P. F. Depta, T. Konstandin, K. Schmidt-Hoberg, and C. Tasillo (2023), 2306.09411.
- [21] E. Madge, E. Morgante, C. P. Ibáñez, N. Ramberg, W. Ratzinger, S. Schenk, and P. Schwaller (2023), 2306.14856.
- [22] S.-Y. Guo, M. Khlopov, X. Liu, L. Wu, Y. Wu, and B. Zhu (2023), 2306.17022.
- [23] N. Kitajima, J. Lee, K. Murai, F. Takahashi, and W. Yin (2023), 2306.17146.
- [24] Y. Bai, T.-K. Chen, and M. Korwar (2023), 2306.17160.
- [25] S. Blasi, A. Mariotti, A. Rase, and A. Sevrin (2023), 2306.17830.
- [26] J. Ellis, M. Lewicki, C. Lin, and V. Vaskonen (2023), 2306.17147.
- [27] Z. Wang, L. Lei, H. Jiao, L. Feng, and Y.-Z. Fan (2023), 2306.17150.
- [28] N. Kitajima and K. Nakayama (2023), 2306.17390.
- [29] G. Lazarides, R. Maji, and Q. Shafi (2023), 2306.17788.
- [30] S. Vagnozzi (2023), 2306.16912.
- [31] G. Franciolini, A. Iovino, Junior., V. Vaskonen, and H. Veermäe (2023), 2306.17149.
- [32] Y.-F. Cai, X.-C. He, X. Ma, S.-F. Yan, and G.-W. Yuan (2023), 2306.17822.
- [33] V. K. Oikonomou (2023), 2306.17351.
- [34] J. Yang, N. Xie, and F. P. Huang (2023), 2306.17113.
- [35] J. Ellis, M. Fairbairn, G. Hütsi, J. Raidal, J. Urrutia, V. Vaskonen, and H. Veermäe (2023), 2306.17021.
- [36] Z.-Q. Shen, G.-W. Yuan, Y.-Y. Wang, and Y.-Z. Wang (2023), 2306.17143.
- [37] A. Ghoshal and A. Strumia (2023), 2306.17158.
- [38] T. Broadhurst, C. Chen, T. Liu, and K.-F. Zheng (2023), 2306.17821.
- [39] K. Inomata, K. Kohri, and T. Terada (2023), 2306.17834.
- [40] P. F. Depta, K. Schmidt-Hoberg, and C. Tasillo (2023), 2306.17836.
- [41] Y. Gouttenoire and E. Vitagliano (2023), 2306.17841.
- [42] H.-L. Huang, Y. Cai, J.-Q. Jiang, J. Zhang, and Y.-S. Piao (2023), 2306.17577.
- [43] G. Lambiase, L. Mastrototaro, and L. Visinelli (2023), 2306.16977.
- [44] Y. Li, C. Zhang, Z. Wang, M. Cui, Y.-L. S. Tsai, Q. Yuan, and

- Y.-Z. Fan (2023), 2306.17124.
- [45] G. Franciolini, D. Racco, and F. Rompineve (2023), 2306.17136.
- [46] A. D. Linde, Nucl. Phys. B **216**, 421 (1983), [Erratum: Nucl.Phys.B 223, 544 (1983)].
- [47] J. Ellis, M. Lewicki, and J. M. No, JCAP **04**, 003 (2019), 1809.08242.
- [48] P. Athron, C. Balázs, A. Fowlie, L. Morris, and L. Wu (2023), 2305.02357.
- [49] M. Breitbach, J. Kopp, E. Madge, T. Opferkuch, and P. Schwaller, JCAP **07**, 007 (2019), 1811.11175.
- [50] J. Ellis, M. Lewicki, J. M. No, and V. Vaskonen, JCAP **06**, 024 (2019), 1903.09642.
- [51] C. Caprini et al., JCAP **04**, 001 (2016), 1512.06239.
- [52] M. Hindmarsh, S. J. Huber, K. Rummukainen, and D. J. Weir, Phys. Rev. D **92**, 123009 (2015), 1504.03291.
- [53] J. R. Espinosa, T. Konstandin, J. M. No, and G. Servant, JCAP **06**, 028 (2010), 1004.4187.
- [54] H.-K. Guo, K. Sinha, D. Vagie, and G. White, JCAP **01**, 001 (2021), 2007.08537.
- [55] P. Binetruy, A. Bohe, C. Caprini, and J.-F. Dufaux, JCAP **06**, 027 (2012), 1201.0983.
- [56] M. Ibe, S. Kobayashi, Y. Nakayama, and S. Shirai, JHEP **03**, 198 (2022), 2112.11096.
- [57] A. M. Sirunyan et al. (CMS), Phys. Lett. B **793**, 520 (2019), 1809.05937.
- [58] J. de Blas et al., JHEP **01**, 139 (2020), 1905.03764.
- [59] Y. Tan et al., Chin. Phys. C **44**, 123001 (2020), 2001.05912.
- [60] A. Ishikawa, PoS **LeptonPhoton2019**, 147 (2019), 1909.07537.
- [61] C. Potter, A. Steinhebel, J. Brau, A. Pryor, and A. White (2022), 2203.08330.
- [62] C. L. Wainwright, Comput. Phys. Commun. **183**, 2006 (2012), 1109.4189.
- [63] Y. Bai and M. Korwar, Phys. Rev. D **105**, 095015 (2022), 2109.14765.
- [64] S. Deng and L. Bian (2023), 2304.06576.
- [65] J. Liu, L. Bian, R.-G. Cai, Z.-K. Guo, and S.-J. Wang, Phys. Rev. Lett. **130**, 051001 (2023), 2208.14086.
- [66] J. Liu (2023), 2305.15100.
- [67] P. S. B. Dev, R. N. Mohapatra, and Y. Zhang, JCAP **08**, 003 (2020), [Erratum: JCAP 11, E01 (2020)], 2005.00490.
- [68] M. Hufnagel, K. Schmidt-Hoberg, and S. Wild, JCAP **11**, 032 (2018), 1808.09324.
- [69] P. F. Depta, M. Hufnagel, and K. Schmidt-Hoberg, JCAP **04**, 011 (2021), 2011.06519.
- [70] J. R. Espinosa, T. Konstandin, and F. Riva, Nucl. Phys. B **854**, 592 (2012), 1107.5441.